symmetry

MDPI

Article

Heuristic Technique for the Search of Interception Trajectories to Asteroids with the Use of Solar Sails

Lucas Gouvêa Meireles [1,†], Antônio Fernando Bertachini de Almeida Prado [1,2,*,†], Cristiano Fiorilo de Melo [3,†] and Maria Cecília Pereira [3,†]

[1] Postgraduate Division, National Institute for Space Research (INPE), Av. dos Astronautas, 1758, São José dos Campos 12227-900, SP, Brazil
[2] Academy of Engineering, RUDN University, Miklukho-Maklaya Street 6, 117198 Moscow, Russia
[3] Department of Mechanical Engineering, Federal University of Minas Gerais, Av. Antônio Carlos, 6627, Belo Horizonte 31270-901, MG, Brazil
* Correspondence: antonio.prado@inpe.br
† These authors contributed equally to this work.

Abstract: With the advances of space-exploration technologies, a long-lasting concern is finally being addressed: the deflection of potentially hazardous objects (PHOs). Most recently, the first mission of this kind was launched by NASA—the Double Asteroid Redirection Test (DART). Nevertheless, it is estimated that a great number of these PHOs are unattainable by means of current chemical propulsion systems. With that in mind, this study proposes the development of a heuristic technique for the search of interception trajectories with the use of solar sails and its application in determining a set of possible trajectories to intercept hazardous asteroids. As a case study, a hybrid mission inspired by the DART mission is proposed by using a solar sail as means of propulsion after the initial chemical combustion. The dynamics consider a model of the solar radiation pressure acceleration as a function of the orientation of the sail. In turn, the orientation is defined by the application of the developed heuristic technique with the goal of defining alternative trajectories compared to the original mission. These trajectories result in different impact conditions and mission durations. Although the use of solar sails breaks the symmetry in the solutions, the results obtained offer the possibility of fuel economy or even better deflection results by the achievement of greater impact energy with the hazardous objects.

Keywords: asteroid deflection; DART mission; heuristic technique; orbital mechanics; solar sailing

Citation: Meireles, L.G.; Prado, A.F.B.d.A.; de Melo, C.F.; Pereira, M.C. Heuristic Technique for the Search of Interception Trajectories to Asteroids with the Use of Solar Sails. *Symmetry* **2023**, *15*, 617. https://doi.org/10.3390/sym15030617

Academic Editor: Alexander Zaslavski

Received: 7 February 2023
Revised: 23 February 2023
Accepted: 25 February 2023
Published: 1 March 2023

1. Introduction

The development of vehicles capable of absorbing the linear momentum of sunlight and utilizing this gain in energy as its own form of propulsion has opened up a wide range of new possibilities for space trajectories. These vehicles are known as solar sail spacecrafts and make use of this phenomenon as a means of propulsion, thereby, taking advantage of an abundant source of energy in the interplanetary medium of our Solar System: Solar Radiation Pressure (SRP). In this way, some trajectories that were unimaginable in the past using traditional methods of propulsion, such as chemical rocket engines, have begun to be conceived as viable options.

A few space agencies and organizations havealready turned their attention to this technology and started implementing missions of their own throughout the last decade in order to explore the advances that these vehicles make possible and also to aid in their development. A first example is the IKAROS (Interplanetary Kite-craft Accelerated by Radiation Of the Sun) mission, from Japan Aerospace Exploration Agency (JAXA). It was the first mission to deploy and control a solar sail in an interplanetary trajectory [1–5].

The National Aeronautics and Space Administration (NASA) has also ventured into the development of solar sails. Its first mission NanoSail-D, in 2008, never achieved orbit

due to a rocket launch failure [6]. Its replacement mission NanoSail-D2, launched 2 years later, achieved the successful deployment of a 10 m^2 solar sail [7]. Following NASA's solar sail project and with a partnership intention, The Planetary Society conducted the LightSail project. They sought to demonstrate the viability of solar sailing as a mean of propulsion for CubeSats in Low Earth Orbit (LEO). A total of two missions were performed: LightSail-1, in May of 2015 [8], and LightSail-2, in June of 2019 [9–13].

The success in development and demonstrations of solar sail capabilities has promoted the scheduling of a set of new missions from NASA. NEA-Scout, launched in November of 2022, but lost after deployment, would be the first CubeSat to reach and perform reconnaissance of an asteroid [14,15]. ACS3 (Advanced Composite Solar Sail System), scheduled for no earlier then 2023, will test the employment of a new material for lighter and more resistant sail booms, made from a carbon fiber reinforced polymer [16–18]. If successful, NASA expects that this technology will allow the construction of sails up to 2000 m^2 in area [19]. Solar Cruiser, scheduled for 2025, will deploy a 1650 m^2 wide solar sail employed to maintain an artificial orbit around the Lagrange point L1 of the Sun–Earth system [20].

In parallel, space agencies have started to address an issue related to our planetary defense capabilities. The deflection of potentially hazardous objects (PHOs) has long been a desire of humanity. Most recently, NASA was responsible for the Double Asteroid Redirection Test (DART) mission, which aimed to demonstrate the ability of current space technology in changing the orbit of an asteroid [21,22]. It successfully promoted the kinetic impact of a spacecraft into the smaller body of the double asteroid system 65,803 Didymos and a change in its trajectory [23].

With the growing advances of solar-sail technologies and interest in its mission applications [24–27], alongside with the recent planetary defense progress with the success of the DART mission, this study proposes the development of a heuristic technique for the search of interception trajectories to predetermined targets with the use of solar sails. This type of spacecraft breaks the symmetry obtained from Keplerian orbits but offers the possibility of propellant-less propulsion and low-cost trajectories.

The heuristic is meant to facilitate the search for the sail orientation throughout a mission, while guaranteeing a target interception at a given moment in time. This serves as an alternative to conventional methods already in use [28,29]. It is able to determine fast solutions for any target position in a tridimensional space while having a fixed given transfer time. The technique works with ideal [30] or nonideal [31,32] solar sail models and with constant [33] or incident-angle dependent [34] optical coefficients.

The heuristic focuses on establishing distinct stages of operation that maintain a fixed sail orientation, which reduces the number of attitude maneuvers necessary throughout a mission. On the other hand, the given target can be an asteroid, such as a mission focused on deflecting its trajectory, or the proximity of a celestial object, as a part of a mission that requires a gravity assist maneuver or a mission focused on performing a reconnaissance of that object. This study focuses on the application of the heuristic on the first case: an asteroid as a target. Finally, after a description of the heuristic technique and a brief demonstration of its application, a simulation with similar conditions to the DART mission was proposed as a case study. A major difference was the main source of propulsion from the spacecraft, which uses a solar sail to propel itself in its heliocentric orbit into a collision course with the Didymos system.

2. Solar Sailing

The solar sailing dynamics are described in a Spacecraft Oriented Frame (SOF) and taken from Vulpetti et al. [7]. The sail is assumed to have a thin reflective surface with constant mechanical and optical properties throughout the mission. Alternative sail models have been presented by McInnes [35], Dachwald et al. [36], Vulpetti et al. [37].

A representation of the SOF is shown in Figure 1. The origin of the SOF is located at the spacecraft barycenter. Its X-axis points in the same direction of the incoming sunlight

(**u**). This means that it corresponds to the outwards radial direction of the Heliocentric Inertial Frame (HIF). The Z-axis points in the direction of the heliocentric orbital angular momentum of the spacecraft (**h**). Finally, the Y-axis is defined as a consequence of a dextrorotatory system.

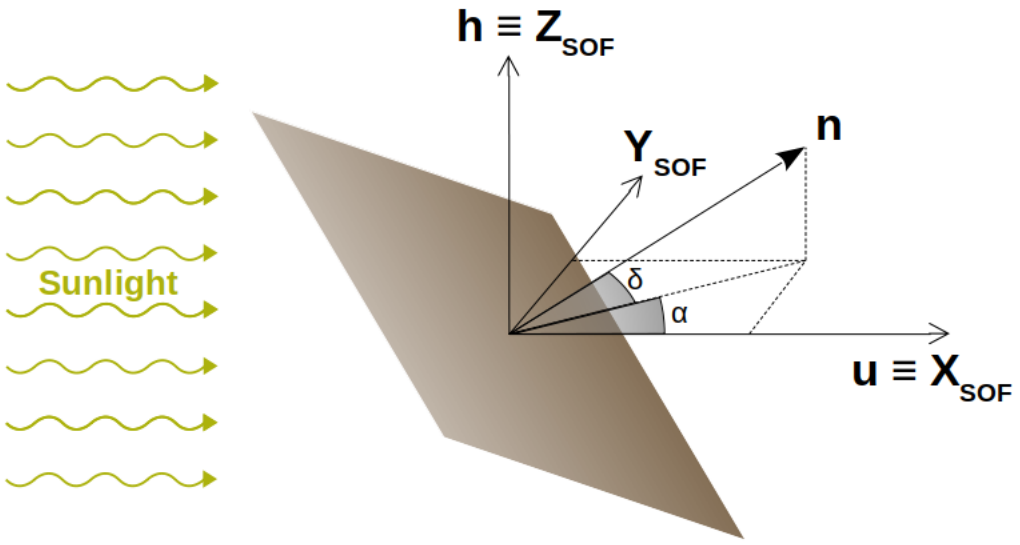

Figure 1. Spacecraft Oriented Frame (SOF).

A unit vector normal to the surface of the solar sail (**n**) is used to represent its orientation. It is defined from two orientation angles: the azimuth (α) and the elevation (δ). The first is the angle between the projection of **n** on the X–Y plane ($proj_{XY}\mathbf{n}$) and **u**. The second is the angle between **n** and $proj_{XY}\mathbf{n}$. Both can be seen in Figure 1.

The resulting SRP acceleration from the solar sail is determined from a lightness vector (**L**), defined as the current SRP acceleration normalized by the local gravitational acceleration of the Sun:

$$\mathbf{L} = \left(\frac{1}{2}\frac{\sigma_c}{\sigma}\right) n_x \left[\left(2r_{spec}n_x + \chi_f r_{diff} + \kappa a_{bsor}\right)\mathbf{n} + \left(a_{bsor} + r_{diff}\right)\mathbf{u}\right] \quad (1)$$

where $\sigma_c \equiv 1.5368\,g/m^2$ is a constant named critical loading and σ is the sail loading, defined from Equation (2). It is the ratio between the spacecraft total mass (m_{sc}) and the surface area of the solar sail (A_{sail}). Additionally, n_x is the projection of **n** on the X-axis. The remaining variables are optical coefficients related to the specular reflectance (r_{spec}), the diffuse reflectance (r_{diff}), the absorptance (a_{bsor}) and the emission/diffusion (χ). The subscript "f" refers to the "front side" of the solar sail, which is the side exposed to the sunlight. Finally, κ is a dimensionless factor that results from the net thrust of the absorbed and re-emitted power on both sides of the sail.

$$\sigma \equiv \frac{m_{sc}}{A_{sail}} \quad (2)$$

This study considers the following values for some of the coefficients: $a_{bsor} = 0.12$, $r_{spec} = 0.8272$, $r_{diff} = 0.0528$ and $\kappa = -0.4383$. These values were taken from solar sail models build by the Jet Propulsion Laboratory (JPL) in the early 2000s [33].

The sail loading $\sigma = 7.98\,g/m^2$ considered in the simulations is a consequence of the combination of two solar sails from NASA: a NEA-Scout-inspired mass value of

$m_{sc} = 15.96\,\text{kg}$ with a sail area $A_{sail} = 2\,000\,\text{m}^2$ from the "DCB HIPERSail II" concept [19]. It results in a futuristic lightness number of $\beta \approx 0.192$ (taken from Equation (3)).

$$\beta = \frac{\sigma_c}{\sigma} \tag{3}$$

Although this cannot be assumed as a near-term system [38], from the perspective of recent engineering advances and limitations, it is useful for the demonstration of the heuristic technique developed in this paper.

3. Heuristic Technique

The technique is applied at each step of the integration of the spacecraft trajectory. At each instant t_i of the integration, the following steps are performed to determine the necessary orientation of the solar sail ($\alpha(t_i)$ and $\delta(t_i)$) in order to obtain the interception of the target position ($\mathbf{r}_{target}$) at instant t_F:

- (Step 1) A projection of the position of the spacecraft at instant t_F is made ($\mathbf{r}_{sc}^{HIF}(t_F)$):
  - t_F is the given moment when the interception of the target position has to occur. Consequently, it is the final integration step.
  - From instant t_i to t_F, the spacecraft is considered to have an elliptical heliocentric orbit. In other words, only the gravitational influence of the Sun and a null solar radiation pressure acceleration are considered.
  - This projection serves as a preliminary analysis, at each step t_i, in order to quickly understand the ongoing trajectory of the spacecraft without a solar sail and how the sail must be oriented in order to correct this trajectory into a successful interception.
- (Step 2) A "Final Position-Oriented Frame" (FPOF) is defined from $\mathbf{r}_{sc}^{HIF}(t_F)$:
  - Its origin is the position of the Sun;
  - The X-axis points in the direction of $\mathbf{r}_{sc}^{HIF}(t_F)$.
  - The Z-axis points in the direction of the spacecraft heliocentric angular momentum at t_F ($\mathbf{h}_{sc}^{HIF}(t_F)$). In other words, the fundamental plane of FPOF is the spacecraft osculating orbital plane at t_F.
  - The Y-axis is defined by dextrorotation.
- (Step 3) A set of three "guidance properties" ($P1$, $P2$ and $P3$) are defined as seen in Figure 2:
  - They are defined in respect to $\mathbf{r}_{sc}^{FPOF}(t_F)$ and $\mathbf{r}_{target}^{FPOF}$, both represented in FPOF.
  - In this study, the target position ($\mathbf{r}_{target}$) is the position of the asteroid at t_F ($\mathbf{r}_{ast}(t_F)$).
    - ($P1$): Arc length, along the circumference of a circle with radius equal to 1 au, between $\mathbf{r}_{sc}^{FPOF}(t_F)$ and $proj_{XY}(\mathbf{r}_{ast}^{FPOF}(t_F))$, which is the projection of the asteroid position at t_F onto the X–Y plane.
    - ($P2$): Difference between the magnitudes of $\mathbf{r}_{sc}^{FPOF}(t_F)$ and $\mathbf{r}_{ast}^{FPOF}(t_F)$.
    - ($P3$): Perpendicular distance of $\mathbf{r}_{ast}^{FPOF}(t_F)$ to the X–Y plane.
- (Step 4) Determine the values of $\alpha(t_i)$ and $\delta(t_i)$ as a function of $P1(t_i)$, $P2(t_i)$ and $P3(t_i)$.

An interception at t_F is obtained if $P1(t_F) = P2(t_F) = P3(t_F) = 0$. Nevertheless, a numeric value equal to zero demands great computational power, numerical accuracy and effort in time. A threshold of 1.0×10^3 m for all properties is considered sufficient to guarantee an interception.

The guidance properties were conveniently defined in such a way that the values of α and δ directly influence their behavior. In summary, α is responsible for correcting $P1$ and $P2$, and δ is responsible for correcting $P3$. The strategy responsible for correcting the value of $P1$ is referred to as H1 (H for heuristic). Furthermore, the one responsible for $P2$ is referred to as H2 and $P3$ as H3:

- (H1): If $P1$ is positive $(P1 > 0)$, it is necessary to reduce the spacecraft mean angular orbital velocity, and α must be positive $(\alpha > 0)$. The opposite is true.
- (H2): If $P2$ is positive $(P2 > 0)$, it is necessary to reduce the spacecraft orbital energy, and α must be negative $(\alpha < 0)$. The opposite is true.
- (H3): If $P3$ is non-zero $(P3 \neq 0)$, it is necessary to change the direction of the spacecraft orbital angular momentum with the appropriate δ value $(\delta \neq 0)$ in accordance to $\mathbf{r}_{sc}^{FPOF}(t)$.

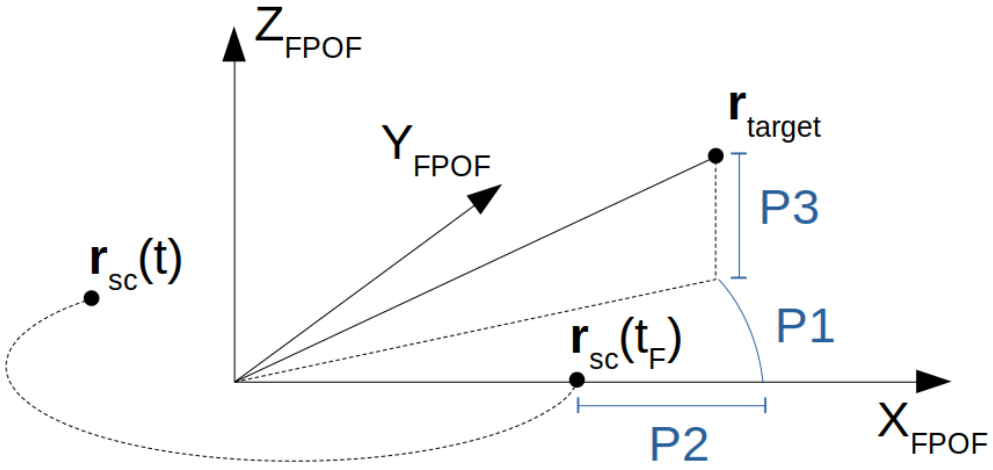

Figure 2. Guidance properties illustration.

It is important to note that H1 interferes with the value of $P2$, and H2 interferes with $P1$, given that both depend on α. Due to that, it is necessary to obtain $P1 = P2 = 0$ at the same time because any correction on one of them affects the value of the other. In order to deal with this problem, H1 and H2 are implemented sequentially. First, the value of $P1$ is corrected with an overshoot (os) compensation, anticipating the effects that H2 will have on its value when correcting $P2$.

The values of α and δ are defined considering an upper boundary of tol_{up}, when a P value needs to be corrected ($|P - os| > tol_{up}$), and a lower boundary of tol_{lw}, when a P value no longer needs correction ($|P - os| < tol_{lw}$). Within a given interval $[tol_{lw}, tol_{up}]$ in which the absolute value of any property $|P - os|$ is inside its range, a weight factor w is calculated (Equation (4)) to determine the value of the angles α and δ in order to guarantee a smooth convergence of P. Overall, their values are determined by Equation (5).

$$w = \log_{10}\left(\frac{|P - os|}{tol_{lw}}\right) / \log_{10}\left(\frac{tol_{up}}{tol_{lw}}\right) \tag{4}$$

$$(\alpha, \delta) = \begin{cases} \theta_{up} & , \text{if } |P - os| > tol_{up} \\ (\theta_{up} - \theta_{lw})w + \theta_{lw} & , \text{if } tol_{lw} < |P - os| < tol_{up} \\ \theta_{lw} & , \text{if } |P - os| < tol_{lw} \end{cases} \tag{5}$$

The values of θ_{lw} and θ_{up} depend on the initial conditions of the simulation, the target position, the interception moment and the sail characteristics. They are established by a trial-and-error process, considering the special attributes of solar sail spacecraft trajectories, until a satisfactory interception trajectory is identified. When that happens, refinements are performed by adjusting the values of os.

4. Preliminary Examples

As preliminary examples of the application of the heuristic technique, a total of five similar trajectories were conceived based on a few common properties:

- Spacecraft in a heliocentric orbit with an acting solar sail (with SRP acceleration).
- Initial circular orbit with radius $r_0 = 1$ au.
- Target position at a distance of $r_{target} = 1.5237$ au to the Sun on the opposite direction of the spacecraft initial position (transfer angle of 180°).
- The time of transfer is initially set as equal to a Hohmann transfer with the same initial and final positions ($t_{transf} = t_{hoh} = 258.87$ days).

The integrations were conducted with the use of Cowell's method [39] and by using an explicit Runge–Kutta method of order 5 and a relative tolerance equal to 1×10^{-12}. The forces considered were the mutual gravitational accelerations between the Sun and the spacecraft and the resulting SRP acceleration from the solar sail as described in Section 2.

A series of small variations in the conditions of the trajectories, as listed below, made it possible to produce the five preliminary examples trajectories. Transfers #1–4 have different time durations. Transfer #5 has a target position outside the original plane of orbit with a non-null inclination.

- $t_{transf\#1} = 1.0 \times t_{hoh}$.
- $t_{transf\#2} = 1.05 \times t_{hoh}$.
- $t_{transf\#3} = 0.95 \times t_{hoh}$.
- $t_{transf\#4} = 2.0 \times t_{hoh}$.
- $t_{transf\#5} = 1.0 \times t_{hoh}$ and $i = 2°$.

Figure 3 presents these preliminary example trajectories as well as a zoom in their final positions located in the left side of the plot. This helps in the visualization of a slightly different final position for Transfer #5, given its out-of-plane trajectory.

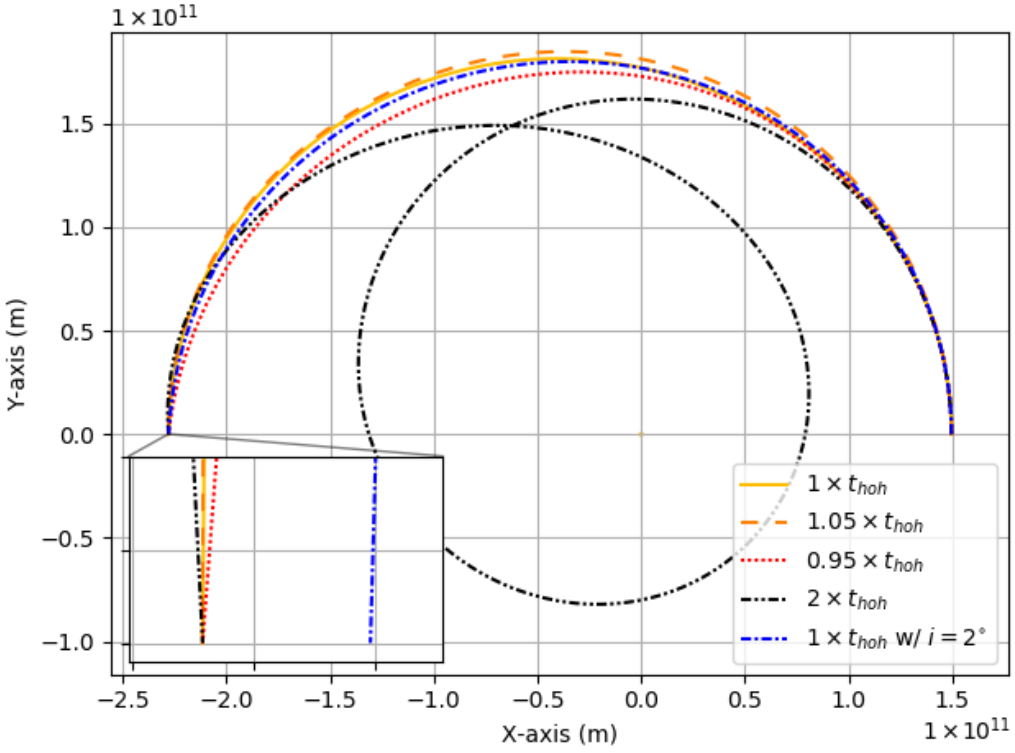

Figure 3. Transfers #1–5 spacecraft heliocentric trajectory with a zoom in the final positions.

Figure 4 displays the evolution of the spacecraft projected final position $\mathbf{r}_{sc}^{HIF}(t_F)$, from Transfer #1, in a red–blue gradient. It starts at the red circle and progresses towards the target position (blue circle) as the solar sail resulting SRP acceleration directs the spacecraft. The dashed black line indicates the spacecraft initial orbit, and the solid line is its actual trajectory.

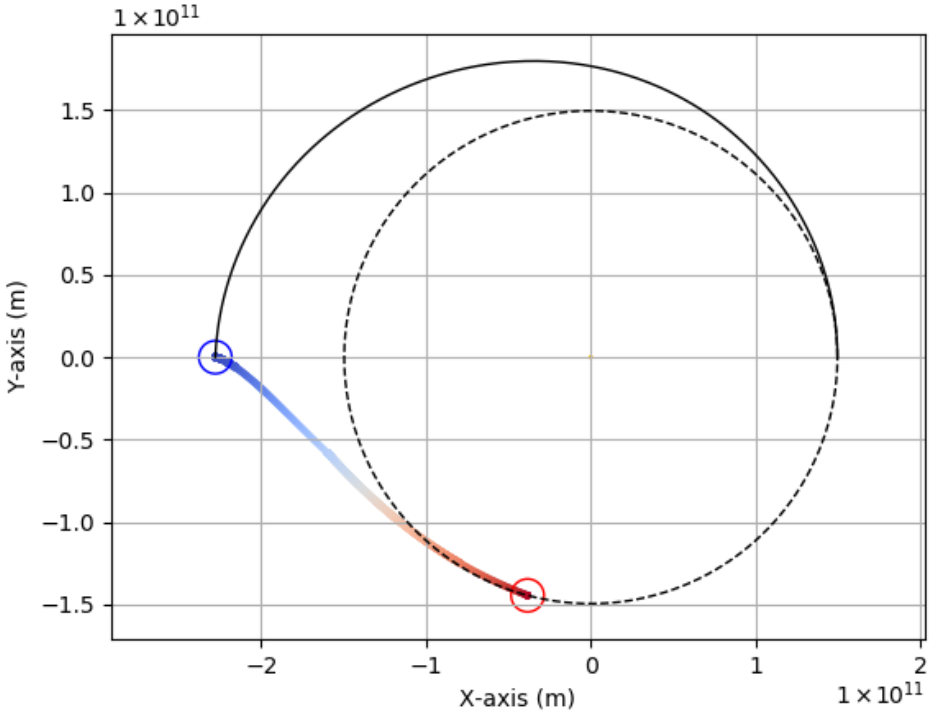

Figure 4. Transfer #1 spacecraft heliocentric trajectory with an evolution of the final position projection.

The change in value for the projected final position is a direct consequence of the sail orientation over time which, in turn, is determined by the application of the heuristic developed in this work.

Upon a quick examination of Figure 3, with the exception of Transfer #4, all of the transfers appear to be quite similar. It is only by examining the sail-orientation angles (α and δ) over time that we perceive how different they are and how important the heuristic is in helping in the calculation of these trajectories. Figures 5 and 6 present these angles, as well as the values of the guidance properties over time, in a linear scale (upper plot) and in a logarithmic scale (middle plot) for Transfers #4 and #5, respectively. These transfers were chosen as representative results with common characteristics among all the solutions obtained. The red dashed line indicates the 1.0×10^3 m interception threshold considered as discussed in Section 3.

Table 1 displays the parameters used to bound the search for the sail azimuth and elevation angles displayed in Figures 5 and 6. They are used in Equation (5) and displayed in an array. These arrays have three components, which correspond to the values used by H1, H2 and H3, respectively.

Table 1. Search parameters.

Transfer	θ_{lw} (°)	θ_{up} (°)	os (m)
#1	$[35, 90, 0]$	$[0, 35, 35]$	$[1.911096915 \times 10^{11}, -11.2 \times 10^3, 0 \times 10^3]$
#2	$[30, 90, 0]$	$[0, 30, 35]$	$[4.627248276 \times 10^{10}, 0.3359 \times 10^6, 0 \times 10^6]$
#3	$[90, 90, 0]$	$[35, 35, 35]$	$[1.926755143 \times 10^{10}, 0.20329 \times 10^6, 0 \times 10^6]$
#4	$[90, 90, 0]$	$[25, 16.3, 35]$	$[3.524816787 \times 10^{11}, 0.5711 \times 10^6, 0 \times 10^6]$
#5	$[35, 90, 0]$	$[10, 35, 20]$	$[5.201761063 \times 10^{10}, 0.911 \times 10^3, 0.229 \times 10^3]$

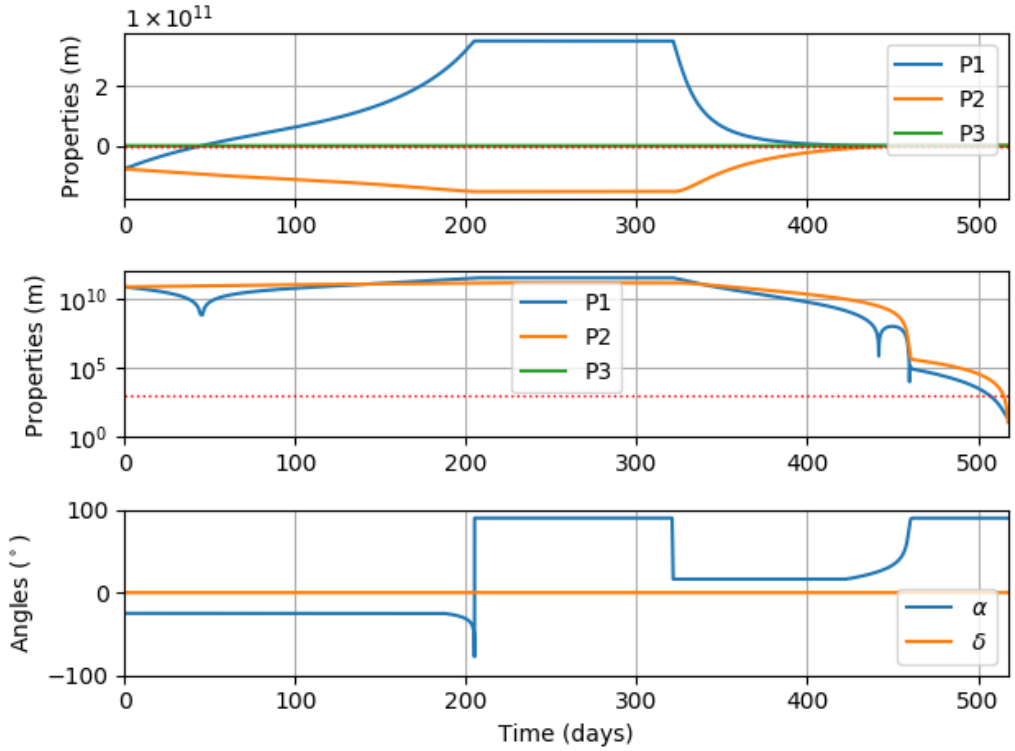

Figure 5. Transfer #4 guidance properties (in linear and logarithmic scale) and sail-orientation angles over time.

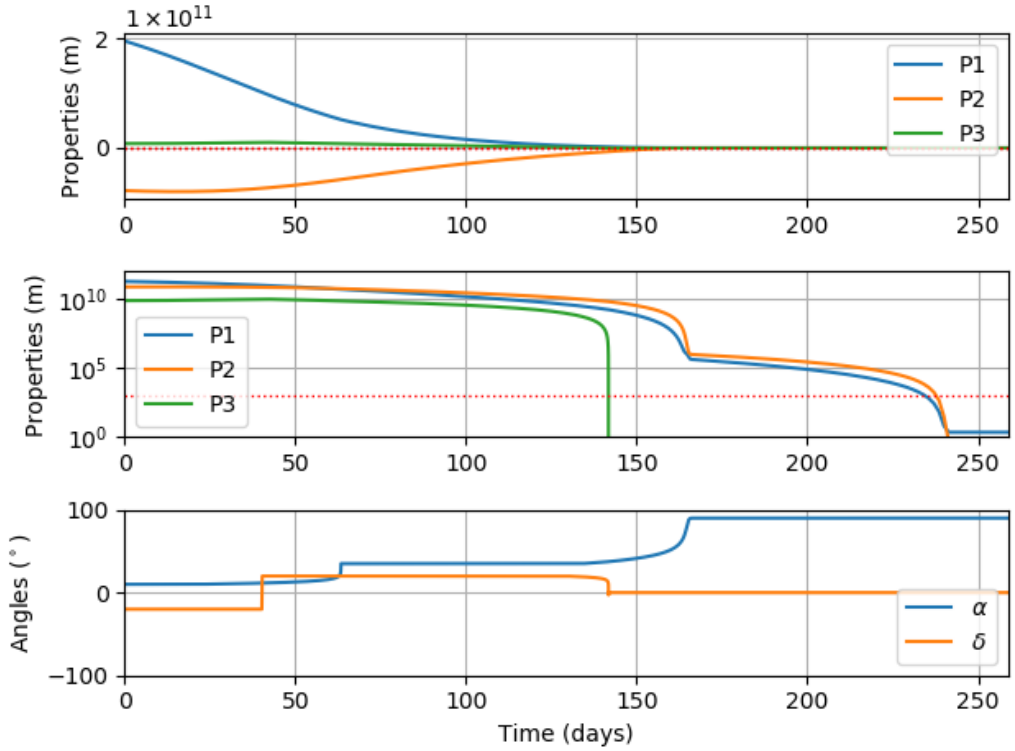

Figure 6. Transfer #5 guidance properties (in linear and logarithmic scale) and sail-orientation angles over time.

Additionally, the values for the lower and upper tolerances were:

- $tol_{lw} = [1.0 \times 10^6, 1.0 \times 10^3, 1.0 \times 10^3]$ m
- $tol_{up} = [1.0 \times 10^{11}, 1.0 \times 10^{10}, 1.0 \times 10^9]$ m

An immediate observation of Figure 5 is the null value of the elevation δ angle during the whole simulation. This is a consequence of the target position already located in the spacecraft initial orbital plane. Consequently, $P3$ is already equal to zero and there is no need for H3 to correct its value. This is not the case for Transfer #5, which needs a correction in $P3$ and, therefore, assumes $\delta \neq 0$ during some part of the simulation. An important observation is due: the value of $\theta_{up} = 35^\circ$ yields the greatest rate of change for $P3$. Nevertheless, a greater value of δ reduces the total solar sail area exposed to sunlight and diminishes the correction effects of $\alpha \neq 0$ in H1 and H2. Transfer #5 is a case where $\theta_{up} = 35^\circ$ was not used exactly for this reason. Instead, a smaller value of $\theta_{up} = 20^\circ$ was chosen as shown in Table 1.

Another common characteristic between these transfers is the H2 with positive azimuth value ($\alpha > 0$). This shows that, as a final correction, they all need an increase in $P2$.

Additionally, it is possible to note that Transfer #5 has an H1 with a positive azimuth value ($\alpha > 0$), which indicates a necessity to reduce the spacecraft mean angular orbital velocity. Additionally, it transitions directly from H1 to H2, with no idle periods of the solar sail ($\alpha = 90^\circ$). This direct H1–H2 transition does not happen in Transfer #4, in which the solar sail remains idle ($\alpha = 90^\circ$) between H1 and H2. Furthermore, Transfer #4 has a negative azimuth during H1. The upper boundary angles θ_{up} of H1 and H2 are crucial to establish a correct balance between the decrease and increase rates of $P1$ and $P2$ in order to reduce both to zero at the same time (the given interception time). It is important to remember that both H1 and H2 change the values of $P1$ and $P2$ simultaneously.

5. Case Study: Didymos System

As a case study, a numeric integration was performed while considering the mutual gravitational interaction between the Sun, the Earth and the solar sail spacecraft, as well as the resulting SRP acceleration from the solar sail. The Didymos system was considered as the target.

The DART mission, from NASA, which also targeted the same asteroid system, was taken as a reference for some of the initial and final dates and, consequently, the positions of the celestial bodies. Simulations considered the date 26 September 2022 at 23:14 h UTC as the interception moment or, in other words, the final time (t_F). A set of five launch dates (initial instant t_0) were considered: the date 24 November 2021 at 06:21 h UTC and one and two months preceding and succeeding this date, which means launches in September, October, November and December of 2021 and January of 2022. These dates were used to take the initial position of the Earth ($\mathbf{r}^{HIF}_{Earth}(t_0)$) and the position of the Didymos system at the given interception moment ($\mathbf{r}^{HIF}_{ast}(t_F)$). The latter is considered to be the target position.

The osculating orbital elements of Earth and Didymos were taken from the database of JPL [40,41] and presented in Table 2.

Table 2. Spacecraft-Didymos relative velocities at interception.

Orb.Elem.	Earth	Didymos
a (au)	1.00000011	1.644324083929969
e	0.01671022	0.3839233231470776
i ($^\circ$)	0.00005	3.407876986118815
Ω ($^\circ$)	−11.26064	73.19326428620921
ω ($^\circ$)	102.94719	319.3188977070352
t_p	2022-Jan-4.161111	2022-Oct-21.76418056

Here, a is the semi-major axis, e is the eccentricity, i is the inclination, Ω is the longitude of the ascending node, ω is the argument of perihelion, and t_p is the time of perihelion passage.

5.1. Earth Escape

Before presenting the achieved results, a section is dedicated for discussing the spacecraft escape from the gravitational sphere of influence of the Earth. This section considers equations from the two-body problem and is not a part of the numerical integrations performed throughout this study. It serves as a preliminary analysis of the necessary increase in velocity to take the spacecraft from a LEO parking orbit into a hyperbolic escape trajectory. In this manner, at the beginning of each numerical integration, the spacecraft is already considered to be away from the Earth at a distance equal to 9.246×10^5 km. This distance is considered to be the limit of the sphere of influence of the Earth (r_{SOI}), from:

$$r_{SOI} = a_{Earth}\left(\frac{m_{Earth}}{m_{Sun}}\right)^{0.4} \tag{6}$$

where a is the semi-major axis and m is the mass.

In order to guarantee its escape from Earth (an orbital energy relative to Earth equal to zero $\varepsilon_{sc}^{Earth} = 0$), its velocity relative to Earth, also considered as its hyperbolic excess velocity (v_{inf}), is taken from:

$$v_{inf} = \sqrt{2\frac{\mu_{Earth}}{r_{SOI}}} \tag{7}$$

where μ is the standard gravitational parameter.

A speed increase (Δv_0) from a circular parking orbit with an initial altitude of $h_0 = 200$ km is then considered to insert the spacecraft into a hyperbolic escape trajectory relative to the Earth where, at a distance of r_{SOI}, the spacecraft will achieve an escape velocity v_{inf}.

$$\Delta v_0 = \frac{h_{hyp}}{r_0} - \sqrt{\frac{\mu_{Earth}}{r_0}} \tag{8}$$

where h_{hyp} is the hyperbolic trajectory specific angular momentum and r_0 is the circular parking orbit radius.

Additionally, the time (t_{esc}) that the spacecraft needs to reach the distance of r_{SOI}, after being inserted into the hyperbolic escape trajectory from the initial circular parking orbit, is also considered:

$$t_{esc} = M_{hyp}\frac{h_{hyp}^3}{\mu_{Earth}^2}\left(e_{hyp}^2 - 1\right)^{-1.5} \tag{9}$$

where M_{hyp} is the hyperbolic mean anomaly at a distance of r_{SOI} and e_{hyp} is the hyperbolic trajectory eccentricity.

For a hyperbolic excess velocity of $v_{inf} = 0.9285$ km/s, which guarantees a minimum escape ($\varepsilon_{sc}^{Earth} = 0$):

- Escape time: $t_{esc} = 6.198505$ days.
- Initial speed increase: $\Delta v_0 = 3.2634$ km/s.

Consequently, the beginning of each numerical integration initializes the bodies at the 30th (not the 24th) of the months considered for launch at 12:08 h UTC.

As a form of comparison, a trajectory taken from a patched conic method [39] was considered without the use of a solar sail, given the same initial circular parking orbit and the start and final dates of the DART mission (24 November 2021 at 06:21 h UTC and 26 September 2022 at 23:14 h UTC, respectively). This trajectory would require a hyperbolic excess velocity of $v_{inf} = 2.9759$ km/s, which would insert the spacecraft into a heliocentric trajectory in a direct collision course with the asteroid system at t_F:

- Initial speed increase: $\Delta v_0 = 3.6195$ km/s.

- Economy: 9.84% (when using a solar sail to reach the asteroid system).

5.2. Interception Trajectories

The trajectories obtained from the heuristic search can be seen in Figure 7.

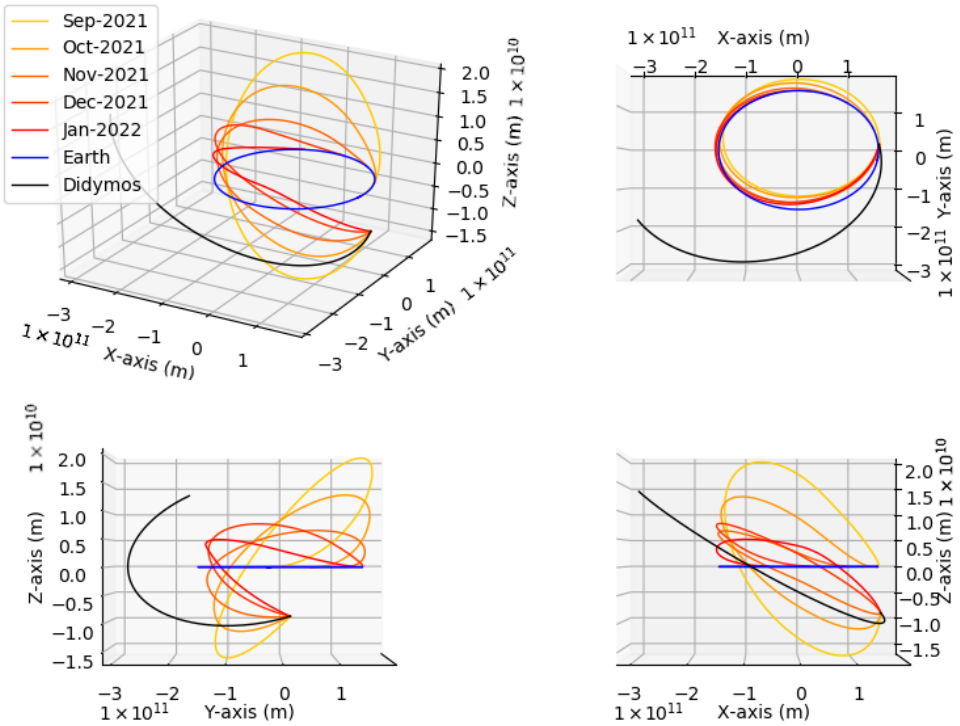

Figure 7. Heliocentric trajectories.

It can be observed that, as a consequence of the parameter setting and, most importantly, the imposed time of flight, the earlier launch dates have the greatest rate of change of the spacecraft orbital plane at the beginning of the transfer. They result in higher inclinations and approach the asteroid from below its own orbital plane. Since they are trajectories that require a longer transfer duration, this could be justified by the establishment of trajectories that go "above and beyond" in distance as a means to delay the time of impact until the specified instant and position are reached.

The latest launch dates result in trajectories with closer passages to the Sun. Specifically, the January 2022 launch presents a swift change in its orbital plane at a closer distance to the target. Not coincidentally, it is at a moment when the spacecraft is at its closest distance to the Sun. This trajectory takes advantage of a larger SRP acceleration at a greater proximity to the Sun in order to perform the inclination change needed in a shorter transfer time.

The parameters used to bound the search are presented in Table 3.

Table 3. Search parameters.

Launch	θ_{lw} (°)	θ_{up} (°)	os (m)
September 2021	$[90, 90, 0]$	$[15, 5, 35]$	$[1.884540031 \times 10^{10}, 0.964420 \times 10^{6}, 4.498857 \times 10^{6}]$
October 2021	$[90, 90, 0]$	$[15, 5, 35]$	$[3.033811596 \times 10^{10}, 1.880184 \times 10^{6}, 8.59387 \times 10^{6}]$
November 2021	$[90, 90, 0]$	$[35, 55, 35]$	$[1.446875557 \times 10^{10}, 1.2367 \times 10^{6}, 3.7153 \times 10^{6}]$
December 2021	$[90, 90, 0]$	$[45, 25, 35]$	$[3.914802412 \times 10^{10}, 2.122068 \times 10^{6}, 1.496168 \times 10^{6}]$
January 2022	$[90, 90, 0]$	$[55, 35, 25]$	$[3.197588329 \times 10^{10}, 1.005404 \times 10^{6}, 1.335357 \times 10^{6}]$

Additionally, the earlier launches of September 2021 and October 2022 required an extra overshoot for H1, equal to $os(1) = 7.832926193 \times 10^{10}$ m. The heuristic search stabilizes $P1$ at this first $os(1)$ and only then at the value presented in Table 3. This was necessary to avoid a quick execution of H1 and a long idle period of the solar sail between H1 and H2. As a consequence, this strategy maintains an area of the sail exposed to sunlight for a longer time, making it possible for H3 to reduce $P3$ to zero.

The values of α and δ from some of the results obtained from the heuristic search, as well as $P1$, $P2$ and $P3$, are presented in Figures 8 and 9.

From Figure 8, it is possible to see the two-step H1 implementation with $P1$ surpassing a null value in great lengths, only to be brought back and stabilized at a closer range of the tolerance region and finally reduced to zero at H2. Additionally, for a launch in November 2021, it is possible to verify that H3 only reduces $P3$ to zero when H2 is being applied. Overall, these transfers present similar operating regimes by having an initial negative azimuth value ($\alpha < 0°$), stabilizing $P1$ at an overshoot target value, going through an idle solar-sail period with null SRP acceleration ($\alpha = 90°$) and switching to H2 with a positive azimuth value ($\alpha > 0°$).

In a November 2021 launch, H3 alternates from an initial positive elevation value ($\delta > 0°$) to a subsequent negative value ($\delta < 0°$). This does not occur with the October 2021 launch, which is able to quickly reduce $P3$ to zero. Another important observation it that the time frame of the plots is in a scale of "years". This means that the seemingly abrupt attitude changes happen in an interval of around 6 to 8 h. At a worst-case scenario, this would mean attitude changes in the order of half a degree per minute ($0.5°/\text{min}$).

Finally, the interception conditions of each transfer is presented in Table 4, when the asteroid has a speed of $|\mathbf{v}_{ast}(t_F)| = 33.996\,\text{km/s}$:

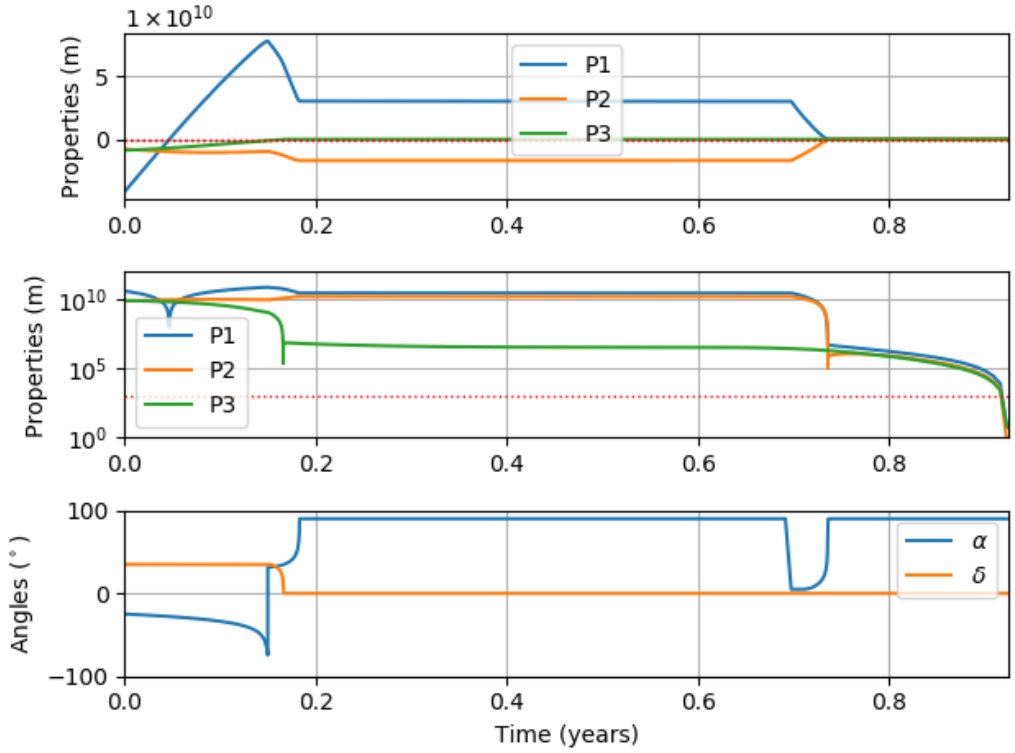

Figure 8. (October 2021) Guidance properties (in linear and logarithmic scale) and sail-orientation angles over time.

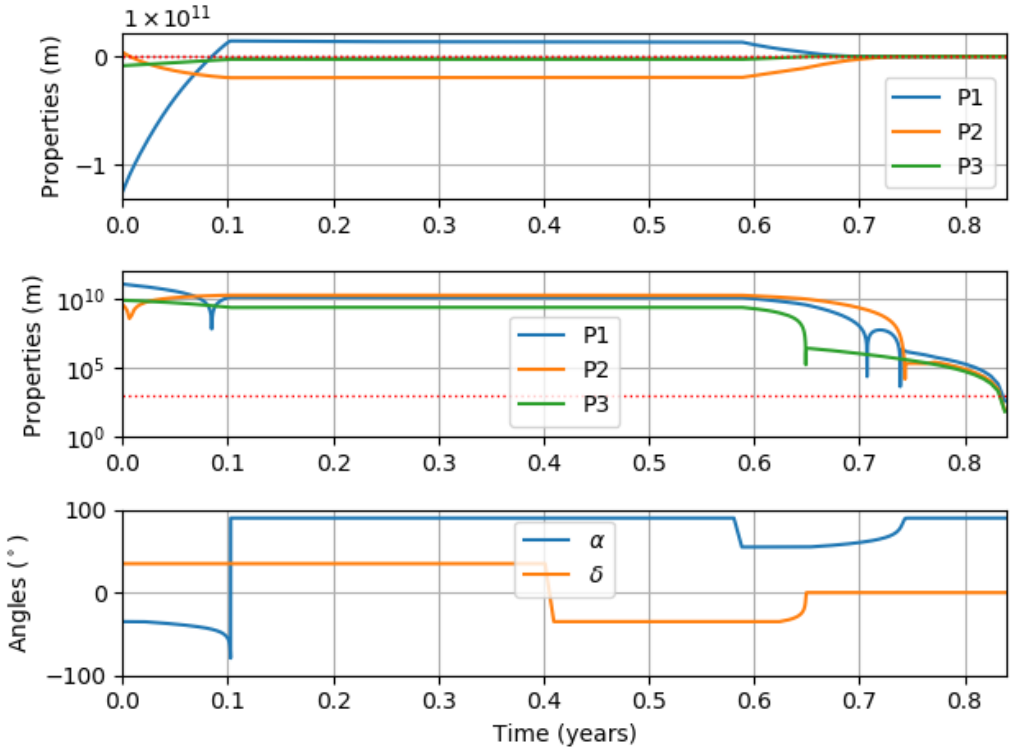

Figure 9. (November 2021) Guidance properties (in linear and logarithmic scale) and sail-orientation angles over time.

Table 4. Spacecraft–Didymos relative velocities at interception.

Launch	$\lvert\mathbf{v}_{sc}(t_F)\rvert$ (km/s)	Δv (km/s)	θ (°)	θ_{xy} (°)	θ_z (°)
Lamb. (November 2021)	28.128	6.434	4.89	4.52	+1.88
September 2021	28.259	11.753	19.05	18.36	+5.15
October 2021	28.350	11.401	18.36	18.21	+2.36
November 2021	30.136	11.091	18.70	18.70	−0.01
December 2021	29.645	11.674	19.65	19.56	−1.94
January 2022	31.620	13.567	23.51	23.34	−2.88

In Table 4, $|\mathbf{v}_{sc}(t_F)|$ is the spacecraft velocity norm at the interception time, $\Delta vs. = |\mathbf{v}_{sc}(t_F) - \mathbf{v}_{ast}(t_F)|$ is the norm of the difference between the velocities of the spacecraft and the asteroid, and θ is the angle between these vectors. Additionally, θ_{xy} is the angle defined in the asteroid orbital plane, and θ_z the angle defined in a plane perpendicular to the asteroid orbital plane.

As expected and visually verified in Figure 7, the two earlier launch dates of September 2021 and October 2021 approach the asteroid from below its orbital plane, resulting in positive θ_z. The opposite (a negative θ_z) occurs for November 2021, December 2021 and January 2022. The largest Δv of January 2022 is mainly due to a higher θ, given the fact that this trajectory has the closest $|\mathbf{v}_{sc}(t_F)|$ value to the asteroid velocity. The lowest Δv of November 2021 is a combination of one of the lowest θ and being the second closest $|\mathbf{v}_{sc}(t_F)|$ to the asteroid. The remaining Δv values are consequences of a balance between the values of $|\mathbf{v}_{sc}(t_F)|$ and θ.

Before ending the analysis of the interception conditions, an important issue should be considered with care. An analysis of the orbit of the asteroid after impact should be performed in order to determine if the interception conditions were indeed successful from a planetary defense point of view. The achieved orbit should result in a safer and farther passage with respect to the Earth.

All of the proposed trajectories present a higher Δv than the value obtained from the patched conic Lambert problem trajectory, calculated and used as a reference for an interception trajectory solely based on chemical propulsion as discussed in Section 5.1. With a goal of obtaining the highest Δv possible, January 2022 is clearly a better scenario, given that it has the highest Δv along with a latter launch date, which gives a longer mission preparation time.

6. Conclusions

In the present paper, we developed a heuristic technique to search for interception trajectories with the use of solar sails. The heuristic focuses on guaranteeing a maximum distance to the target while respecting a given threshold value and a given interception moment. In that manner, it can be employed in a search with restrictions on the final position and the transfer time, though it does not respect any conditions imposed on the interception velocity.

The technique implements distinct regimes of operation for the solar sail, which were conceived to reduce the number of attitude maneuvers necessary throughout a mission. This technique can be used to determine trajectories for spacecrafts propelled by solar sails to intercept an asteroid in a collision course with the Earth, for example. As a case study, a hybrid mission inspired by the DART mission from NASA was proposed with the use of an initial chemical propulsion impulse followed by a solar-sail-propelled trajectory.

Demonstrations of the heuristic technique started as a series of transfers to an arbitrary target at a 1.5237 au distance to the Sun with a transfer angle of 180° and finished as a case study proposing alternative launch dates to intercept the Didymos system. Though simulations made use of an advanced sail loading value, from a technological and engineering perspective, demonstration of the heuristic was successful by proving it was capable of determining interception trajectories that could result in a longer mission-planning time, a 9.84% fuel economy compared to a purely chemical-fuel-propelled spacecraft and a 12.41% greater velocity at impact with the Didymos system.

Author Contributions: Conceptualization, L.G.M. and M.C.P.; methodology, L.G.M.; software, L.G.M.; validation, A.F.B.d.A.P., C.F.d.M. and M.C.P.; formal analysis, A.F.B.d.A.P., C.F.d.M. and M.C.P.; investigation, L.G.M.; resources, A.F.B.d.A.P.; data curation, L.G.M.; writing—original draft preparation, L.G.M. and A.F.B.d.A.P.; writing—review and editing, A.F.B.d.A.P., C.F.d.M. and M.C.P.; visualization, L.G.M., A.F.B.d.A.P., C.F.d.M. and M.C.P.; supervision, A.F.B.d.A.P.; project administration, A.F.B.d.A.P.; funding acquisition, A.F.B.d.A.P. All authors have read and agreed to the published version of the manuscript.

Funding: This research was funded by the National Council for Scientific and Technological Development (CNPq) grant # 309089/2021-2, by the São Paulo Research Foundation (FAPESP) grants # 2016/24561-0 and 2018/19959-0 and by the RUDN University Scientific Projects Grant System, project # 202235-2-000.

Institutional Review Board Statement: Not applicable.

Informed Consent Statement: Not applicable.

Data Availability Statement: The data presented in this study are available on request from the corresponding author.

Acknowledgments: The authors wish to express their appreciation for the support provided by the National Council for the Improvement of Higher Education (CAPES).

Conflicts of Interest: The authors declare no conflict of interest. The funders had no role in the design of the study; in the collection, analyses, or interpretation of data; in the writing of the manuscript; or in the decision to publish the results.

References

1. Tsuda, Y.; Mori, O.; Funase, R.; Sawada, H.; Yamamoto, T.; Saiki, T.; Endo, T.; Yonekura, K.; Hoshino, H.; Kawaguchi, J. Achievement of IKAROS—Japanese deep space solar sail demonstration mission. *Acta Astronaut.* **2013**, *82*, 183–188. [CrossRef]
2. Funase, R.; Kawaguchi, J.; Mori, O.; Sawada, H.; Tsuda, Y. IKAROS, a Solar Sail Demonstrator and Its Application to Trojan Asteroid Exploration. In Proceedings of the 53rd Structures, Structural Dynamics and Materials Conference, AIAA/ASME/ASCE/AHS/ASC, AIAA, Honolulu, HI, USA, 23–26 April 2012. [CrossRef]
3. Mori, O.; Tsuda, Y.; Sawada, H.; Funase, R.; Saiki, T.; Yamamoto, T.; Yonekura, K.; Hoshino, H.; Minamino, H.; Endo, T.; et al. IKAROS and Extended Solar Power Sail Missions for Outer Planetary Exploration. *Trans. Jpn. Soc. Aeronaut. Space Sci. Aerosp. Technol. Jpn.* **2012**, *10*, 413–420. [CrossRef] [PubMed]
4. Tsuda, Y.; Mori, O.; Funase, R.; Sawada, H.; Yamamoto, T.; Saiki, T.; Endo, T.; Kawaguchi, J. Flight status of IKAROS deep space solar sail demonstrator. *Acta Astronaut.* **2011**, *69*, 833–840. [CrossRef]
5. Mori, O.; Sawada, H.; Funase, R.; Morimoto, M.; Endo, T.; Yamamoto, T.; Tsuda, Y.; Kawakatsu, Y.; Kawaguchi, J.; Miyazaki, Y.; et al. First Solar Power Sail Demonstration by IKAROS. *Trans. Jpn. Soc. Aeronaut. Space Sci. Aerosp. Technol. Jpn.* **2010**, *8*, 425–431. [CrossRef] [PubMed]
6. Johnson, L.; Whorton, M.; Heaton, A.; Pinson, R.; Laue, G.; Adams, C. NanoSail-D: A solar sail demonstration mission. *Acta Astronaut.* **2011**, *68*, 571–575. [CrossRef]
7. Vulpetti, G.; Johnson, L.; Matloff, G.L. *Solar Sails*; Copernicus Books: New York, NY, USA, 2015; 277p.
8. Betts, B.; Nye, B.; Vaughn, J.; Greeson, E.; Chute, R.; Spencer, D.; Ridenoure, R.; Munakata, R.; Wong, S.; Diaz, A.; et al. LightSail 1 mission results and public outreach strategies. In Proceedings of the Fourth International Symposium on Solar Sailing, ISSS, Kyoto, Japan, 17–20 January 2017.
9. Spencer, D.A.; Betts, B.; Bellardo, J.M.; Diaz, A.; Plante, B.; Mansell, J.R. The LightSail 2 solar sailing technology demonstration. *Adv. Space Res.* **2021**, *67*, 2878–2889. [CrossRef]
10. Mansell, J.; Spencer, D.A.; Plante, B.; Diaz, A.; Fernandez, M.; Bellardo, J.; Betts, B.; Nye, B. Orbit and Attitude Performance of the LightSail 2 Solar Sail Spacecraft. In Proceedings of the Scitech Forum, AIAA, Orlando, FL, USA, 6–10 January 2020.
11. Betts, B.; Spencer, D.; Bellardo, J.; Nye, B.; Diaz, A.; Plante, B.; Mansell, J.; Fernandez, M.; Gillespie, C.; Garber, D. LightSail 2: Controlled Solar Sailing Using a CubeSat. In Proceedings of the 70th International Astronautical Congress, IAF, Washington, DC, USA, 21–25 October 2019.
12. Plante, B.; Spencer, D.; Betts, B.; Chait, S.; Bellardo, J.; Diaz, A.; Pham, I. LightSail 2 ADCS: From Simulation to Mission Readiness. In Proceedings of the Fourth International Symposium on Solar Sailing, ISSS, Kyoto, Japan, 17–20 January 2017.
13. Betts, B.; Spencer, D.; Nye, B.; Munakata, R.; Bellardo, J.; Wong, S.; Diaz, A.; Ridenoure, R.; Plante, B.; Foley, J.; et al. LightSail 2: Controlled solar sailing using a cubesat. In Proceedings of the Fourth International Symposium on Solar Sailing, ISSS, Kyoto, Japan, 17–20 January 2017.
14. Johnson, L.; Betts, E.; Heaton, A.; Jones, C.; McNutt, L.; Pruitt, M.; Stott, J.; Wallace, D.; Wilson, R.; Castillo-Rogez, J.; et al. Near Earth Asteroid Scout (NEA Scout): Mission update. In Proceedings of the 36th Annual Small Satellite Conference, Logan, UT, USA, 6–11 August 2022.
15. McNutt, L.; Johnson, L.; Kahn, P.; Castillo-Rogez, J.; Frick, A. Near-Earth Asteroid (NEA) Scout. In Proceedings of the Space Conference and Exposition, AIAA, San Diego, CA, USA, 4–7 August 2014.
16. Horner, S.D.; Wilkie, W.K.; Fernandez, J.M.; Brown, P.L.; Fishman, J.L. *Advanced Composite Solar Sail System: Demonstrating Deployable Composite Solar Sails for Future Deep Space Small Spacecraft*; Technical Report; National Aeronautics and Space Administration: Hampton, VA, USA, 2019.
17. Fernandez, J.M.; Rose, G.; Stohlman, O.R.; Younger, C.J.; Dean, G.D.; Warren, J.E.; Kang, J.H.; Bryant, R.G.; Wilkie, K.W. An advanced composites-based solar sail system for interplanetary small satellite missions. In Proceedings of the 2018 AIAA Spacecraft Structures Conference, Kissimmee, FL, USA, 8–12 January 2018; p. 1437.
18. Fernandez, J.M.; Rose, G.K.; Younger, C.J.; Dean, G.D.; Warren, J.E.; Stohlman, O.R.; Wilkie, W.K. NASA's Advanced Solar Sail Propulsion System for Low-Cost Deep Space Exploration and Science Missions that Use High Performance Rollable Composite Booms. In Proceedings of the fourth International Symposium on Solar Sailing, Kyoto, Japan, 17–20 January 2017.
19. Wilkie, W.K. Overview of the NASA Advanced Composite Solar Sail System (ACS3) Technology Demonstration Project. In Proceedings of the AIAA Scitech 2021 Forum, Virtual Event, 11–15 and 19–21 January 2021; p. 1260.
20. Pezent, J.B.; Sood, R.; Heaton, A.; Miller, K.; Johnson, L. Preliminary trajectory design for NASA's Solar Cruiser: A technology demonstration mission. *Acta Astronaut.* **2021**, *183*, 134–140. [CrossRef]
21. Statler, T.S.; Raducan, S.D.; Barnouin, O.S.; DeCoster, M.E.; Chesley, S.R.; Barbee, B.; Agrusa, H.F.; Cambioni, S.; Cheng, A.F.; Dotto, E.; et al. After DART: Using the First Full-scale Test of a Kinetic Impactor to Inform a Future Planetary Defense Mission. *Planet. Sci. J.* **2022**, *3*, 244. [CrossRef]
22. Cheng, A.; Michel, P.; Reed, C.; Galvez, A.; Carnelli, I.; Headquarters, P. Dart: Double asteroid redirection test. In Proceedings of the European Planetary Science Congress, Madrid, Spain, 23–28 September 2012; Volume 7, pp. 23–28.
23. NASA. NASA Confirms DART Mission Impact Changed Asteroid's Motion in Space. Available online: https://www.nasa.gov/press-release/nasa-confirms-dart-mission-impact-changed-asteroid-s-motion-in-space (accessed on 15 November 2022).
24. Gong, S.P.; Li, J.F.; Zeng, X.Y. Utilization of an H-reversal trajectory of a solar sail for asteroid deflection. *Res. Astron. Astrophys.* **2011**, *11*, 1123. [CrossRef]

25. Zeng, X.; Gong, S.; Li, J. Earth-crossing asteroid intercept mission with a solar sail spacecraft. *IEEE Aerosp. Electron. Syst. Mag.* **2014**, *29*, 4–15. [CrossRef]
26. Heiligers, J.; Fernandez, J.; Stohlman, O.; Wilkie, W. Trajectory design for a solar-sail mission to asteroid 2016 HO3. *Astrodynamics* **2019**, *3*, 231–246. [CrossRef]
27. Meireles, L.; Prado, A.; de Melo, C.; Pereira, M. A Study on Different Attitude Strategies and Mission Parameters Based on LightSail-2. *Rev. Mex. De Astron. Y Astrofísica* **2022**, *58*, 23–35. [CrossRef]
28. Wood, L.J.; Bauer, T.P.; Zondervan, K.P. Comment on "Time-Optimal Orbit Transfer Trajectory for Solar Sail Spacecraft". *J. Guid. Control. Dyn.* **1982**, *5*, 221–224. [CrossRef]
29. Peloni, A.; Ceriotti, M.; Dachwald, B. Solar-sail trajectory design for a multiple near-earth-asteroid rendezvous mission. *J. Guid. Control. Dyn.* **2016**, *39*, 2712–2724. [CrossRef]
30. Sauer, C., Jr. Optimum solar-sail interplanetary trajectories. In Proceedings of the Astrodynamics Conference, San Diego, CA, USA, 18–20 August 1976; p. 792.
31. Mengali, G.; Quarta, A.A. Optimal three-dimensional interplanetary rendezvous using non-ideal solar sail. *J. Guid. Control. Dyn.* **2005**, *28*, 173–177. [CrossRef]
32. Meireles, L.G. Analysis of Non-Ideal Attitude Dynamics Models for Solar Sails and Its Effects on the Orbital Movement. Master's Thesis, Instituto Nacional de Pesquisas Espaciais (INPE), São José dos Campos, Brazil, 2019.
33. McInnes, C.R. *Solar Sailing*; Springer: London, UK, 2004. 296p.
34. Scaglione, G.V.S. The Aurora project: Estimation of the optical sail parameters. *Acta Astronaut.* **1999**, *44*, 123–132. [CrossRef]
35. McInnes, C.R. Solar Sailing: Orbital mechanics and mission applications. *Adv. Space Res.* **2003**, *31*, 1971–1980. [CrossRef]
36. Dachwald, B.; Mengali, G.; Quarta, A.A.; Macdonald, M. Parametric model and optimal control of solar sails with optical degradation. *J. Guid. Control. Dyn.* **2006**, *29*, 1170–1178. [CrossRef]
37. Vulpetti, G.; Apponi, D.; Zeng, X.; Circi, C. Wrinkling analysis of solar-photon sails. *Adv. Space Res.* **2021**, *67*, 2669–2687. [CrossRef]
38. Ceriotti, M.; McInnes, C.; Diedrich, B. The pole-sitter mission concept: An overview of recent developments and possible future applications. In Proceedings of the 62nd International Astronautical Congress 2011, Cape Town, South Africa, 3–7 October 2011; Volume 3, pp. 2543–2559.
39. Bate, R.R.; Mueller, D.D.; White, J.E. *Fundamentals of Astrodynamics*; Dover: New York, NY, USA, 1971; 455p.
40. NASA. Earth Fact Sheet. Available online: https://nssdc.gsfc.nasa.gov/planetary/factsheet/earthfact.html (accessed on 30 August 2022).
41. NASA. Small-Body Database Lookup. Available online: https://ssd.jpl.nasa.gov/tools/sbdblookup.html/sstrDidymos (accessed on 30 August 2022).